Nuclear Inst. and Methods in Physics Research, A 918 (2019) 1–8

Contents lists available at ScienceDirect

Nuclear Inst. and Methods in Physics Research, A

journal homepage: www.elsevier.com/locate/nima

Long-term simulation of space-charge effects

Ji Qiang

Lawrence Berkeley National Laboratory, Berkeley, CA 94720, United States

ARTICLE INFO

Keywords:
Space-charge effects
Particle simulation
Symplectic model

ABSTRACT

The long-term macroparticle tracking simulation is computationally challenging but needed in order to study space-charge effects in high intensity circular accelerators. To address the challenge, in this paper, we proposed using a fully symplectic particle-in-cell model for the long-term space-charge simulation. We analyzed the artificial numerical emittance growth in the simulation and suggested using threshold numerical filtering in frequency domain to mitigate the emittance growth in the simulation. We also explored alternative frozen space-charge simulations and observed qualitative agreement with the self-consistent simulations.

1. Introduction

The nonlinear space-charge effects present strong limit on beam intensity in high intensity/high brightness accelerators by causing beam emittance growth, halo formation, and even particle loss. Self-consistent macroparticle simulations have been widely used to study these space-charge effects in the accelerator community [1–14]. In some applications, especially in high intensity circular accelerators such as a synchrotron, one has to track the beam for many turns. It becomes computationally challenging for the long-term space charge tracking simulation since on one hand, one needs to avoid numerical artifacts and to ensure accuracy of the simulation results. On the other hand, one would like to reduce the computing time in physics applications.

The charged particle motion inside an accelerator follows classical Hamiltonian dynamics and satisfies the symplectic conditions. For better accuracy, it is desirable to preserve the symplectic conditions in the long-term numerical tracking simulation too. Violating the symplectic conditions in numerical integration results in unphysical results [15,16]. A gridless symplectic space-charge tracking model and a symplectic particle-in-cell (PIC) model were proposed in recent studies [17,18].

Even with the use of the symplectic space-charge model, there still exists artificial emittance growth in long-term space-charge simulations. This numerical emittance growth could be due to numerical collisional effects associated with the use of smaller number of macroparticles in the simulation compared with the real number of particles inside the beam [19–23]. In this study, we analyzed the numerical emittance growth in simulations using the symplectic spectral PIC model and proposed a threshold filtering method to mitigate the numerical emittance growth. In order to improve computational speed in the long-term space-charge simulation, we also explored a frozen space-charge model in the simulation.

The organization of this paper is as follows: after the introduction, we present the symplectic particle-in-cell space-charge model in Section 2; we analyzed the numerical emittance growth in self-consistent macroparticle tracking and its mitigation in Section 3; we tested the non-self consistent frozen space-charge simulations in Section 4; and drew conclusions in Section 5.

2. Symplectic particle-in-cell space-charge model

In the self-consistent symplectic particle-in-cell (PIC) model, macroparticle phase space coordinate advancing through a single step τ can be given as:

$$\begin{aligned}\zeta(\tau) &= \mathcal{M}(\tau)\zeta(0)\\ &= \mathcal{M}_1(\tau/2)\mathcal{M}_2(\tau)\mathcal{M}_1(\tau/2)\zeta(0) + O(\tau^3)\end{aligned} \tag{1}$$

where the transfer map $\mathcal{M}_1$ corresponds to the single particle Hamiltonian including external fields and the transfer map $\mathcal{M}_2$ corresponds to the space-charge potential from the multi-particle Coulomb interactions. The numerical integrator Eq. (1) will be symplectic if both the transfer map $\mathcal{M}_1$ and the transfer map $\mathcal{M}_2$ are symplectic. For a coasting beam inside a rectangular perfectly conducting pipe, the space-charge potential can be obtained from the solution of the Poisson equation using a spectral method [18]. The one-step symplectic transfer map $\mathcal{M}_2$ of particle i from the space-charge Hamiltonian is given as:

$$x_i(\tau) = x_i(0) \tag{2}$$

$$y_i(\tau) = y_i(0) \tag{3}$$

$$\begin{aligned}p_{xi}(\tau) &= p_{xi}(0) - \tau 4\pi K \sum_I \sum_J \frac{\partial S(x_I - x_i)}{\partial x_i} \times \\ &\quad S(y_J - y_i)\phi(x_I, y_J)\end{aligned} \tag{4}$$

$$\begin{aligned}p_{yi}(\tau) &= p_{yi}(0) - \tau 4\pi K \sum_I \sum_J S(x_I - x_i) \times \\ &\quad \frac{\partial S(y_J - y_i)}{\partial y_i}\phi(x_I, y_J)\end{aligned} \tag{5}$$

E-mail address: jqiang@lbl.gov.

https://doi.org/10.1016/j.nima.2018.11.114
Received 6 October 2018; Received in revised form 20 November 2018; Accepted 26 November 2018
Available online 6 December 2018

where both p_{xi} and p_{yi} are normalized by the reference particle momentum p_0, $K = qI/(2\pi\epsilon_0 p_0 v_0^2\gamma_0^2)$ is the generalized perveance, I is the beam current, ϵ_0 is the permittivity of vacuum, p_0 is the momentum of the reference particle, v_0 is the speed of the reference particle, γ_0 is the relativistic factor of the reference particle, $S(x)$ is the unitless shape function (also called deposition function in the PIC model), and ϕ denotes the interaction potential between grid point I and J and is given as:

$$\phi(x_I, y_J) = \frac{4}{ab}\sum_{l=1}^{N_l}\sum_{m=1}^{N_m}\frac{1}{\gamma_{lm}^2}\sum_{I'}\sum_{J'}\bar{\rho}(x_{I'}, y_{J'})\times \sin(\alpha_l x_{I'})\sin(\beta_m y_{J'})\sin(\alpha_l x_I)\sin(\beta_m y_J) \quad (6)$$

where a and b are the horizontal (x) and the vertical (y) aperture sizes respectively, $\alpha_l = l\pi/a$, $\beta_m = m\pi/b$, $\gamma_{lm}^2 = \alpha_l^2 + \beta_m^2$, the integers I, J, I', and J' denote the two dimensional computational grid index, and the summations with respect to those indices are limited to the range of a few local grid points depending on the specific deposition function. The density related function $\bar{\rho}(x_{I'}, y_{J'})$ on the grid can be obtained from:

$$\bar{\rho}(x_{I'}, y_{J'}) = \frac{1}{N_p}\sum_{j=1}^{N_p} S(x_{I'} - x_j)S(y_{J'} - y_j), \quad (7)$$

In the PIC literature, compact shape functions are used in the simulation. For example, a quadratic shape function can be written as [24,25]:

$$S(x_I - x_i) = \begin{cases} \frac{3}{4} - (\frac{x_i - x_I}{\Delta x})^2, & |x_i - x_I| \le \Delta x/2 \\ \frac{1}{2}(\frac{3}{2} - \frac{|x_i - x_I|}{\Delta x})^2, & \Delta x/2 < |x_i - x_I| \\ & \le 3/2\Delta x \\ 0 & \text{otherwise} \end{cases} \quad (8)$$

$$\frac{\partial S(x_I - x_i)}{\partial x_i} = \begin{cases} -2(\frac{x_i - x_I}{\Delta x})/\Delta x, & |x_i - x_I| \le \Delta x/2 \\ (-\frac{3}{2} + \frac{(x_i - x_I)}{\Delta x})/\Delta x, & \Delta x/2 < |x_i - x_I| \\ & \le 3/2\Delta x, \quad x_i > x_I \\ (\frac{3}{2} + \frac{(x_i - x_I)}{\Delta x})/\Delta x, & \Delta x/2 < |x_i - x_I| \\ & \le 3/2\Delta x, \quad x_i \le x_I \\ 0 & \text{otherwise} \end{cases} \quad (9)$$

where Δx is the mesh size in x dimension. The same shape function and its derivative can be applied to the y dimension. The explicit shape function and its derivative in the above equations results from the requirement of the symplectic condition [18].

Using the symplectic transfer map $\mathcal{M}_1$ for the single particle Hamiltonian including external fields from a magnetic optics code [26–28] and the transfer map $\mathcal{M}_2$ for space-charge Hamiltonian, one obtains a symplectic PIC model including the self-consistent space-charge effects.

3. Numerical emittance growth in long-term simulation

In the long-term macroparticle space-charge tracking simulation, even with the use of self-consistent symplectic space-charge model, there still exists numerical emittance growth. To study this effect, we used a 1 GeV kinetic energy proton beam transporting inside a lattice that consists of 10 focusing-drift-defocusing-drift (FODO) lattice periods and one sextupole element per turn. The horizontal and the vertical aperture sizes are 6.5 mm. A schematic plot of the lattice is shown in Fig. 1. The zero current tune of the lattice is 2.417. With 30 A beam current, the corresponding linear space-charge tune shift is 0.113. When the sextupole strength is set to zero, the lattice is a purely linear FODO lattice. When the sextupole strength is nonzero, it can excite nonlinear resonance which will be further enhanced by the space-charge effects.

Fig. 1. Schematic plot of a periodic FODO and sextupole lattice.

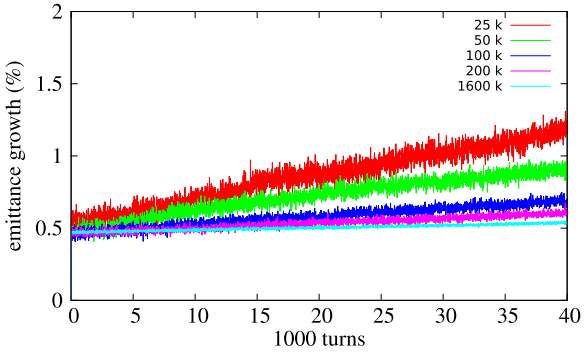

Fig. 2. The 4D emittance growth evolution in a FODO lattice using 25, 50, 100, 200, and 1600 thousand macroparticles in the simulation.

Fig. 2 shows the four dimensional (4D) emittance growth $(\frac{\epsilon_x}{\epsilon_{x0}}\frac{\epsilon_y}{\epsilon_{y0}} - 1)\%$ evolution of the 1 GeV, 30 A current proton beam through 40,000 turns of the above lattice with zero sextupole strength and using 25,000, 50,000, 100,000, 200,000, and 1.6 million macroparticles and 64×64 spectral modes. The initial 0.5% jump of emittance growth is due to charge redistribution to match into the lattice. It is seen that with the increase of the number of macroparticles, the emittance growth decreases. With the use of 1.6 million macroparticles, there is little emittance growth which is expected in this linear lattice. The extra emittance growth with smaller number of macroparticles is a numerical artifact.

The cause of this numerical artifact can be understood using a one-dimensional model. Following the spectral method used in the above symplectic PIC model for the space-charge potential, we calculated the sine function expansion mode amplitude from a smooth density distribution function on the grid and from a macroparticle sampled distribution function depositing onto the grid. Here, the amplitude of density mode l from the sampled macroparticle deposition is given as:

$$\rho^l = \frac{1}{N_p}\frac{2}{N_g\Delta x}\sum_i\sum_I S(x_I - x_i)\sin(\alpha_l x_i) \quad (10)$$

where N_p is the total number of macroparticles and N_g is the total number of grid cells. Fig. 3 shows the mode amplitude as a function of mode number from the smooth Gaussian function on the grid, from the linear particle deposition, from the quadratic particle deposition, and from the Gaussian kernel particle deposition on the grid using 25,000 macroparticles and 128 grid cells. Here, the Gaussian kernel particle deposition shape function is defined as:

$$S(x_I - x_i) = \begin{cases} \exp(-\frac{(x_i - x_I)^2}{2\sigma^2}); & |x_i - x_I| \le 3.5\sigma \\ 0; & \text{otherwise} \end{cases} \quad (11)$$

and σ is the chosen as the mesh size.

It is seen that for the smooth Gaussian distribution function, with mode number beyond 20, the mode amplitude is nearly zero while the mode amplitude from the macroparticle deposition fluctuates with a magnitude of about 10^{-4}. Those nonzero high frequency modes cause fluctuation in density distribution and induce extra numerical emittance growth. The high frequency mode fluctuation amplitude becomes smaller from the linear deposition, to the quadratic deposition, and to the Gaussian kernel deposition. The difference between the linear

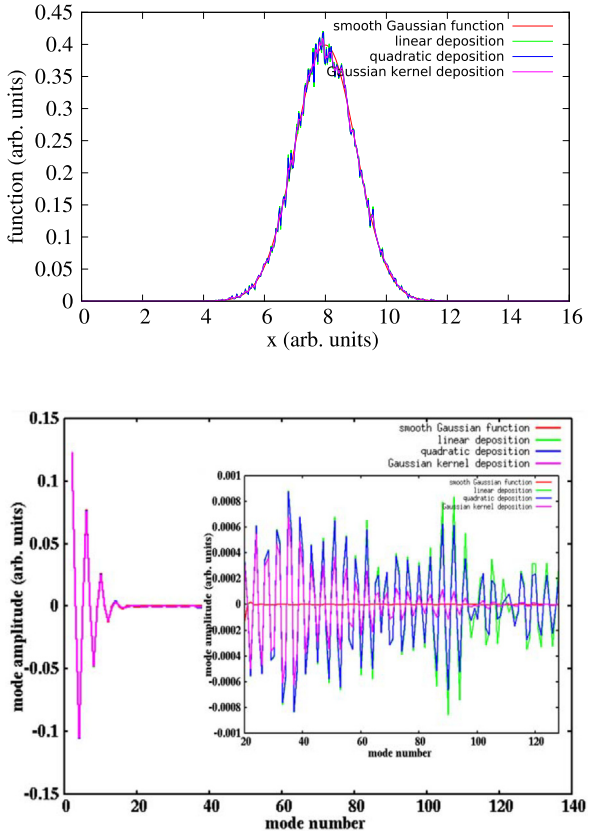

Fig. 3. A Gaussian function (top), and its spectral mode amplitude (bottom) as a function of mode number from the smooth Gaussian function on the grid (red), from the linear particle deposition (green), the quadratic particle deposition (blue), and the Gaussian kernel particle deposition on the grid (magenta) using 25,000 macroparticles and 128 grid cells. The small plot inside the bottom figure is a zoom-in plot for mode number between 20 and 128 . (For interpretation of the references to color in this figure legend, the reader is referred to the web version of this article.)

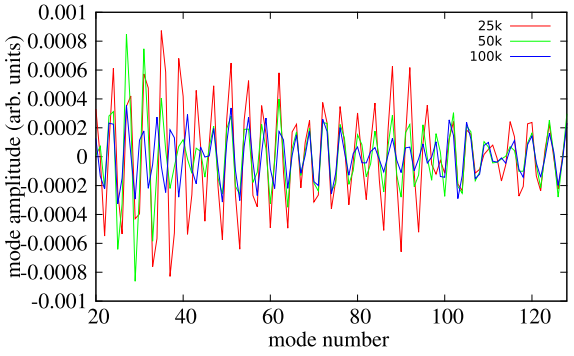

Fig. 4. Mode amplitude of the Gaussian function as a function of mode number from the quadratic particle deposition using 25,000 (red), 50,000 (green) and 100,000 (blue) macroparticles and 128 grid cells . (For interpretation of the references to color in this figure legend, the reader is referred to the web version of this article.)

deposition and the quadratic deposition is small. The Gaussian kernel deposition shows significantly smaller fluctuation for mode number greater than 60 since it corresponds to the infinite limit order of the polynomial deposition function [29]. The higher order deposition scheme spreads the macroparticle across multiple grid points and reduces the density fluctuation. However, the Gaussian kernel deposition is computationally more expensive in comparison to the other two deposition methods. It involves a number of exponential function evaluations (eight in this example) for each macroparticle and is a factor of about seven

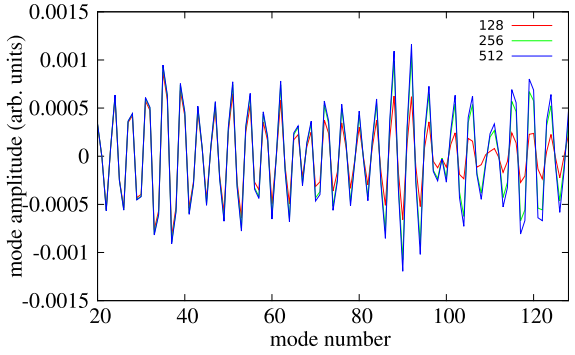

Fig. 5. Mode amplitude of the Gaussian function as a function of mode number from the quadratic particle deposition using 25,000 and 128, 256 and 512 grid cells.

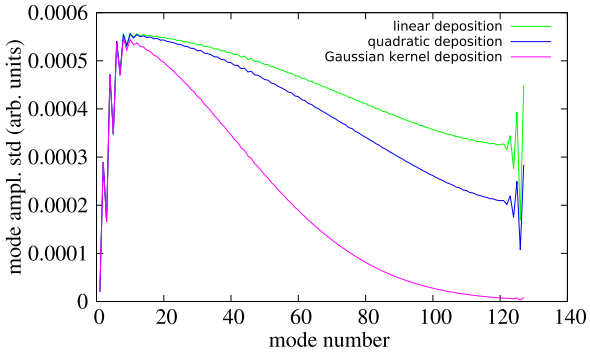

Fig. 6. Mode amplitude standard deviation as a function of mode number from the linear particle deposition (green), the quadratic particle deposition (blue), and the Gaussian kernel particle deposition on the grid (magenta) using 25,000 macroparticles and 128 grid cells . (For interpretation of the references to color in this figure legend, the reader is referred to the web version of this article.)

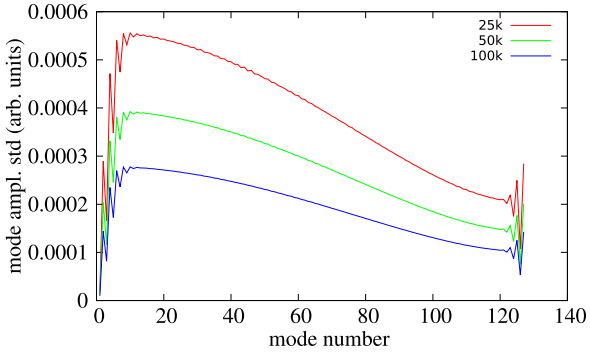

Fig. 7. Mode amplitude standard deviation as a function of mode number from the quadratic particle deposition using 25,000 (red), 50,000 (green) and 100,000 (blue) macroparticles and 128 grid cells . (For interpretation of the references to color in this figure legend, the reader is referred to the web version of this article.)

(or about five after some function optimization to reduce the number of exponential function evaluation) slower than the quadratic deposition in this one dimensional example.

The mode amplitude fluctuation from macroparticle deposition depends on the number of macroparticles used to sample the density distribution and the number of grid points. Fig. 4 shows the mode amplitude of the Gaussian function as a function of mode number (≥20) from the quadratic deposition using 25,000, 50,000, and 100,000 macroparticles and 128 grid cells. With the increase of the number of macroparticles, the mode amplitude fluctuation becomes smaller. For a fixed macroparticle number, the mode amplitude fluctuation also depends on the number of grid cells used in the deposition. Fig. 5 shows

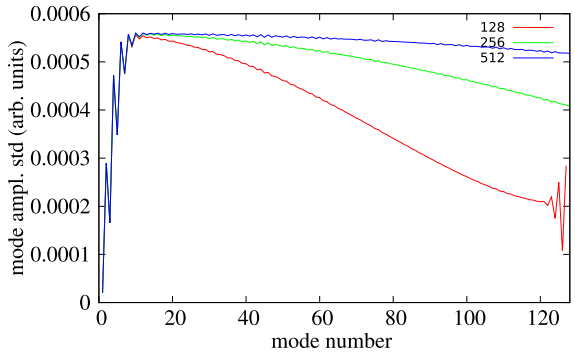

Fig. 8. Mode amplitude standard deviation as a function of mode number from the quadratic particle deposition using 25,000 and 128, 256 and 512 grid cells.

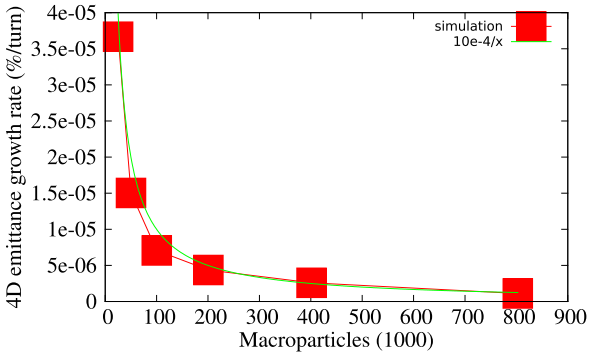

Fig. 9. The 4D emittance growth rate as a function of the simulation macroparticle number using the FODO lattice.

the mode amplitude of the Gaussian function as a function of mode number (≥20) from the quadratic deposition using 128, 256, and 512 grid cells and 25,000 macroparticles. As the number of grid cells increases, the mode amplitude fluctuation becomes larger especially towards the larger mode number (≥70). The larger mesh size of less grid cell helps smooth out high frequency fluctuation.

The above fluctuation of the density mode amplitude from macroparticle deposition can be estimated quantitatively using the standard deviation (or variance) of the mode amplitude. Given the mode amplitude ρ^l in Eq. 10, the variance of ρ^l is given as:

$$var(\rho^l) = \frac{1}{N_p} var(\frac{2}{N_g \Delta x} \sum_I S(x_I - x_i)\sin(\alpha_l x_i)) \tag{12}$$

where

$$var(\frac{2}{N_g \Delta x} \sum_I S(x_I - x_i)\sin(\alpha_l x_i)) \approx \frac{1}{N_p}(\frac{2}{N_g \Delta x})^2 \sum_i [\sum_I S(x_I - x_i) \times \sin(\alpha_l x_i)]^2 - (\rho^l)^2 \tag{13}$$

From the variance of each mode amplitude, one can calculate the standard deviation (std) of each mode amplitude by taking the square root of the variance. Fig. 6 shows the mode amplitude standard deviation as a function of mode number for the above Gaussian function by using the linear deposition, the quadratic deposition, and the Gaussian kernel deposition. The mode amplitude standard deviation is small at small mode number and grows quickly to 10^{-4} level and start to decrease after about 10 modes. The standard deviation among the three deposition schemes becomes smaller as the order of deposition scheme becomes higher. The Gaussian kernel deposition shows least mode amplitude standard deviation which is consistent with the results in Fig. 3.

In Fig. 7, we show the mode amplitude standard deviation as a function of mode number using 25,000, 50,000, and 100,000 macroparticle sampling of the Gaussian distribution. The standard deviation decreases

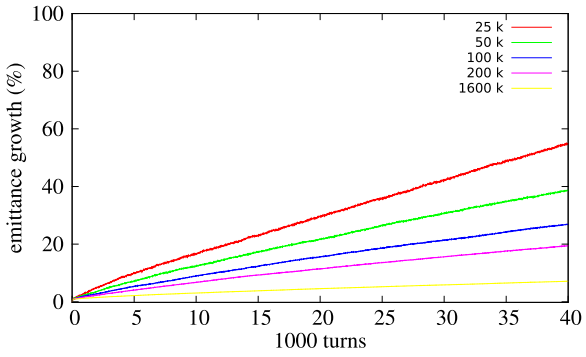

Fig. 10. The 4D emittance growth evolution in the FODO and sextupole lattice using 25, 50, 100, 200, and 1600 thousand macroparticles in the simulation.

with the increase of the macroparticle number and scales as $1/\sqrt{N_p}$ as expected from Eq. (12). Fig. 8 shows the mode amplitude standard deviation as a function of mode number using 128, 256, and 512 grid cells and 25,000 macroparticles for the above Gaussian distribution. For small mode number (less than 10), the standard deviation is close among three numbers of grid cells. For larger mode number, the standard deviation of the small number of grid cells is smaller, which is also seen in Fig. 5.

The error in the charge density mode amplitude results in error in the solution of space-charge potential and the corresponding force in momentum update in Eqs. (4)–(5). Assume that the error of force in x momentum update is δF, after one step τ, i.e. $x_2 = x_1$, $x_2' = x_1' + \delta F \tau$, the new emittance under the effect of this force will be:

$$\begin{aligned}\epsilon_2^2 &= \langle x_2^2\rangle\langle x_2'^2\rangle - \langle x_2 x_2'\rangle^2 \\ &= \langle x_1^2\rangle\langle x_1'^2\rangle - \langle x_1 x_1'\rangle^2 + \\ &\quad 2(\langle x_1^2\rangle\langle x_1'\delta F\rangle - \langle x_1 x_1'\rangle\langle x_1\delta F\rangle)\tau + (\langle x_1^2\rangle\langle \delta F^2\rangle - \langle x_1\delta F\rangle^2)\tau^2\end{aligned} \tag{14}$$

where $\langle\rangle$ denotes the average with respect to the particle distribution. The above equation can be rewritten as:

$$\begin{aligned}\epsilon_2^2 &= \epsilon_1^2 + \\ &\quad 2(\langle x_1^2\rangle\langle x_1'\delta F\rangle - \langle x_1 x_1'\rangle\langle x_1\delta F\rangle)\tau + (\langle x_1^2\rangle\langle \delta F^2\rangle - \langle x_1\delta F\rangle^2)\tau^2\end{aligned} \tag{15}$$

and the emittance growth due to this error will be:

$$\Delta\epsilon \approx (\langle x^2\rangle\langle x'\delta F\rangle - \langle xx'\rangle\langle x\delta F\rangle)\tau/\epsilon + \frac{1}{2}(\langle x^2\rangle\langle(\delta F)^2\rangle - \langle x\delta F\rangle^2)\tau^2/\epsilon \tag{16}$$

If δF is a linear function of the position x, the emittance growth will be zero as expected since the linear force will not change the beam emittance. If δF is a random error force with zero mean and independent of x and x', the emittance growth would be

$$\frac{\Delta\epsilon}{\tau} \approx \frac{1}{2}\langle x^2\rangle\langle(\delta F)^2\rangle\tau/\epsilon \tag{17}$$

which is in agreement with the result of Ref. [23]. Assume that this error is due to mode amplitude fluctuation of the finite number of macroparticles sampling, from the above example, we see that $\langle(\delta F)^2\rangle \propto 1/N_p$. This suggests that the numerical emittance growth would decrease as more macroparticles are used. If δF is not a purely random error force (e.g. due to systematic truncation error), the dependence of the emittance growth on the number of macroparticle is more complicated. Fig. 9 shows the 4D emittance growth rate as a function of macroparticle number in the linear FODO lattice using 256×256 grid cells. It is seen that the emittance growth rate scales as $1/N_p$, which agrees well with the scaling of the random sample fluctuation induced emittance growth.

In the above example, we used a linear FODO lattice with zero sextupole strength. When the sextupole strength is nonzero, it can excite third order resonance. Fig. 10 shows the 4D emittance growth evolution of the 30 A proton beam inside a lattice with an effective $10/m/m$ integrated sextupole strength using several macroparticle numbers and

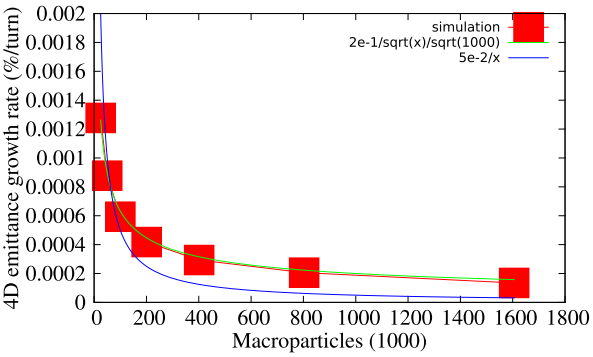

Fig. 11. The 4D emittance growth rate as a function of macroparticle number using the FODO and sextupole lattice.

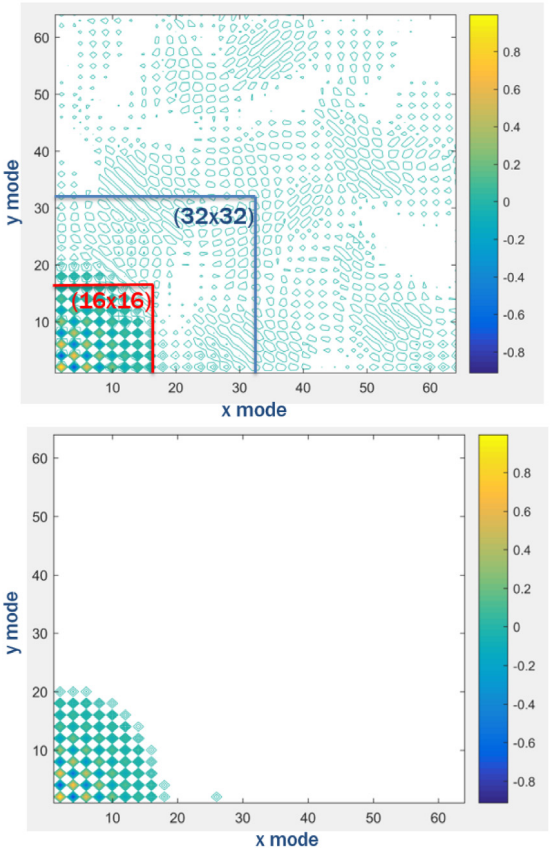

Fig. 12. The mode amplitude of a 2D Gaussian distribution without (top) and with 1% threshold filter (bottom).

64 × 64 modes. Besides the physical emittance growth caused by the resonance, there also exists significant numerical emittance growth due to the finite macroparticle sampling. Fig. 11 shows the emittance growth rate in this case as function of the macroparticle number. It appears that in this case, the emittance growth rate scales close to $1/\sqrt{N_p}$. This slower scaling with respect to the N_p might be due to the interaction between the numerical force error and the nonlinear resonance.

The charge density fluctuation from the macroparticle sampling can be further smoothed out by using a numerical filter in frequency domain besides employing the shape function for particle deposition. As seen from the above one-dimensional example, the shape function helps suppress high frequency errors. However, even with the use of the shape function, there still exists significant level of mode amplitude error fluctuation for mode number greater than 20. Those mode amplitude

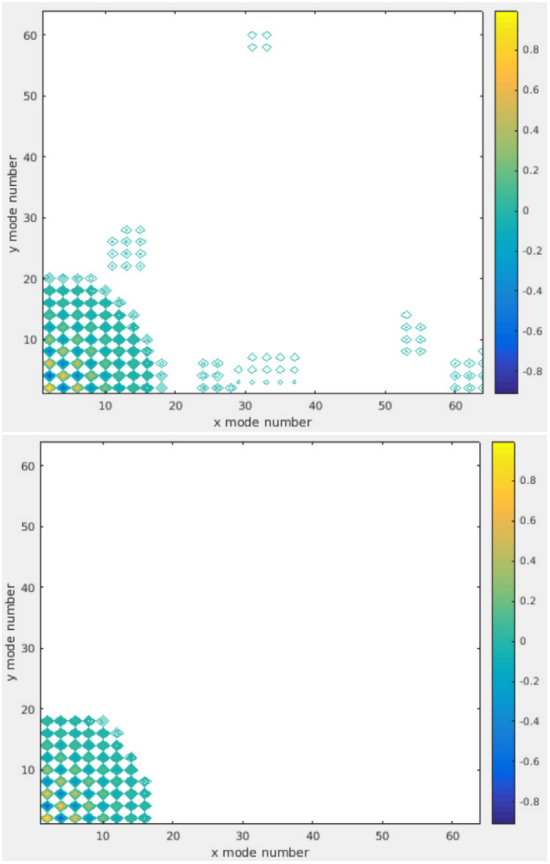

Fig. 13. The mode amplitude of a 2D Gaussian distribution with two sigma standard deviation (top) and with four sigma standard deviation threshold filter (bottom).

errors can be removed by numerical filtering in the frequency domain. Instead of using a standard cut-off method that removes all modes beyond a given mode number (i.e. cut-off frequency), we proposed using an amplitude threshold method to remove unwanted modes. The mode with an amplitude below the threshold value is removed from the density distribution. The advantage of this method is instead of removing all high frequency modes, it will keep the high frequency modes with large amplitudes. These modes can represent real physics structures inside the beam. The threshold also removes the unphysical low frequency modes associated with the small number of macroparticle sampling. Here, we explored two threshold methods. In the first threshold method, the threshold value is calculated from a given fraction of the maximum amplitude of the density spectral distribution. In the second method, the threshold value is defined as a few standard deviations of the mode amplitude as shown in the one-dimensional Gaussian function example. The mode with an amplitude below the threshold value is regarded as numerical sampling error due to the use of small number of macroparticles and is removed from the density distribution. The advantage of the first method is that the threshold value is readily attainable from the density spectral distribution. The disadvantage of this method is that the threshold fraction is an external supplied hyperparameter. The advantage of the second method is that the threshold value is calculated dynamically through the simulation. The disadvantage of this method is the computational cost to obtain the standard deviation of each mode. The total computational cost of those standard deviations is proportional to the number of modes multiplied by the number of macroparticles. This makes computing the mode amplitude standard deviations more expensive than computing the mode amplitudes (proportional to the number of macroparticles) and not affordable at every time step. In practice, these mode amplitude

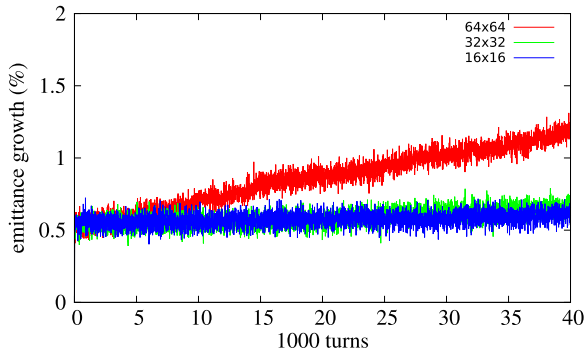

Fig. 14. The 4D emittance growth with 64 × 64, 32 × 32, 16 × 16 modes cut-off filtering of the charge density distribution using 25k in the FODO lattice.

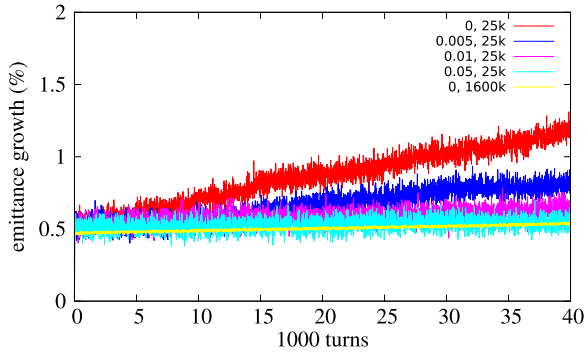

Fig. 15. The 4D emittance growth with 0 (no filtering) with 0.005, 0.01 and 0.05 threshold filtering of charge density distribution using 25k macroparticles and 0 filtering using 1600k macroparticles in the FODO lattice.

standard deviations can be computed once (or once in while) during the simulation and reused in the following simulation. Fig. 12 shows the spectral amplitude of a 2D Gaussian density distribution without and with 0.01 threshold filter using 128 × 128 grid cells and 25,000 macroparticles with the quadratic deposition method. The standard cut-off filter with 16 × 16 and 32 × 32 modes are also indicated in above plot. Most high frequency noise is removed in this distribution by using the threshold filtering method. Fig. 13 shows the above sampled spectral amplitude distribution by using the threshold values of two-sigma standard deviation and four-sigma standard deviation. The two-sigma standard deviation threshold value does not remove all the higher frequency errors.

As a test of the threshold filtering method, we reran the above space-charge long-term simulation in the linear FODO lattice using 0 (no filtering), 0.005, 0.01 and 0.05 threshold filtering the charge density in the simulation and 25,000 macroparticles and the brute force direct cut-off filtering. Here, the larger threshold value, the less number of modes will be included in the simulation. Those results are shown in Figs. 14–15. It is seen that without numerical filtering, there is significant emittance growth after 40,000 turns. With 0.05 threshold filtering, there is little emittance growth, which is consistent with the expected physics emittance growth by using 1600k macroparticles without filtering. Both the brute force filtering and the threshold filtering work well in this case.

We also reran the simulation of 30A proton beam transport in a lattice including nonlinear sextupole element shown in Fig. 10. The 4D emittance growth evolutions using the brute force cut-off and the threshold filtering are shown in Fig. 16. It is seen that even with 16 × 16 mode cut-off filtering, there still exists significant emittance growth, while a threshold value 0.1 helps significantly lower the emittance growth. Using the four-sigma standard deviation threshold value yields similar emittance growth to the fraction threshold (0.1) as shown in Fig. 17. The amplitude threshold filtering works better than the cut-off

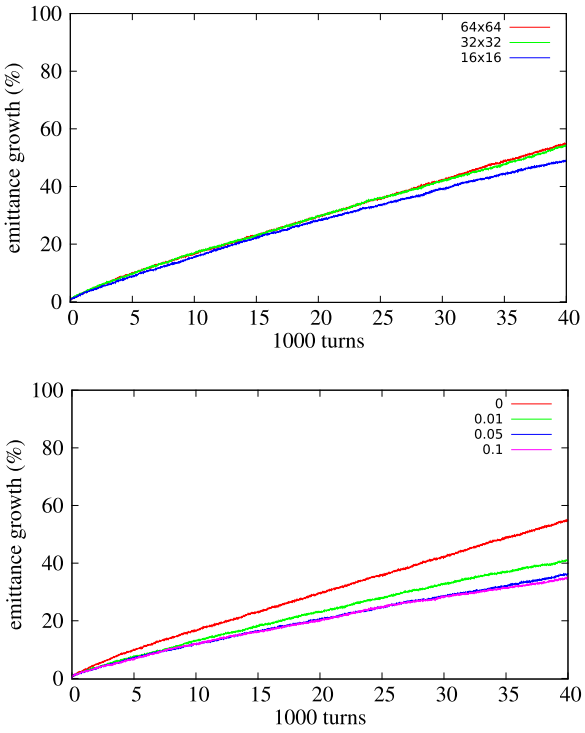

Fig. 16. The 4D emittance growth using 64 × 64, 32 × 32, 16 × 16 modes (top) and with 0 (no filtering) with 0.01, 0.05 and 0.1 threshold filtering (bottom) of charge density distribution using 25k macroparticles in a FODO and sextupole lattice.

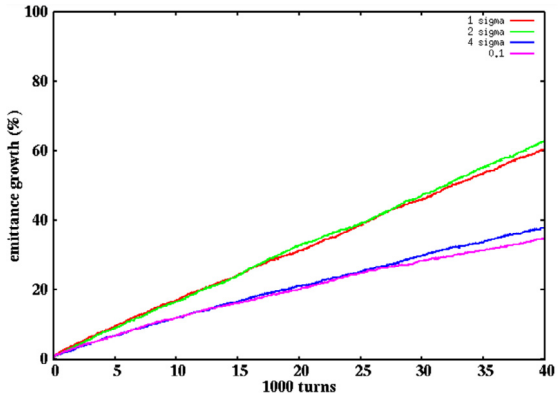

Fig. 17. 4D emittance growth with one sigma, two sigma, four sigma standard deviation and 0.1 maximum amplitude threshold filtering of charge density distribution using 25k macroparticles in a FODO and sextupole lattice.

filtering in this case because it removes not only the unwanted high frequency errors but also the unwanted low frequency errors, while the cut-off filtering removes only the high frequency errors. Those low frequency errors interact with the nonlinear resonance and cause extra emittance growth.

4. Frozen space-charge simulation

In order to improve computational speed in the long-term simulation, we also explored a frozen space-charge model during the simulation [30–32]. Here, instead of self-consistently updating the space-charge calculation at every time step, after some initial time steps, we store the solutions of the space-charge potential along the lattice and reuse those stored space-charge potentials for the following long-term simulation. This model assumes that after some initial time steps, the charge density distribution will not vary significantly from turn to turn.

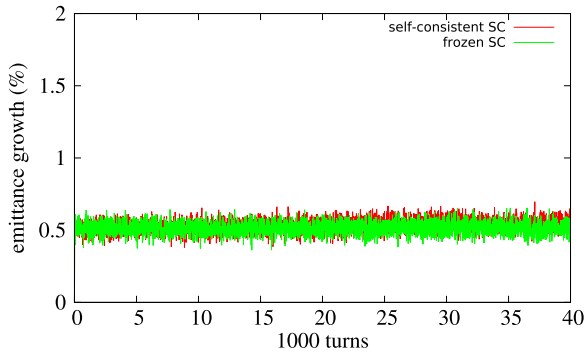

Fig. 18. The 4D emittance growth evolution from the self-consistent simulation (red) and the frozen space-charge simulation (green) in a FODO lattice.

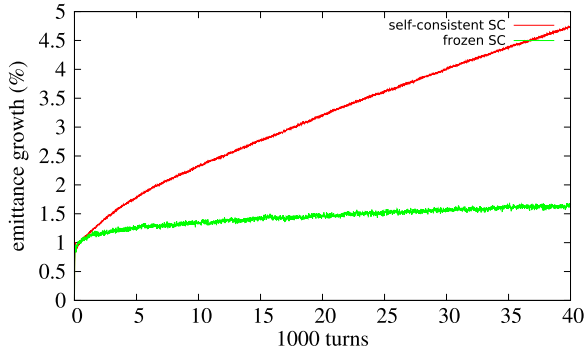

Fig. 19. The 4D emittance growth evolution from the self-consistent simulation (red) and the frozen space-charge model (green) in a FODO and sextupole lattice.

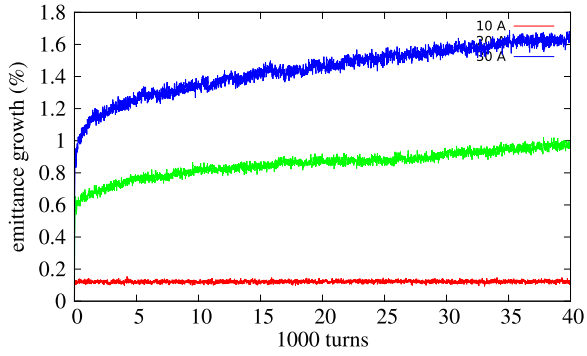

Fig. 20. The 4D emittance growth evolution from the frozen space-charge model simulation with 10 A, 20 A and 30 A beam currents in a FODO and sextupole lattice.

Fig. 18 shows the total 4D emittance growth evolution inside the above linear FODO lattice example from the simulation using the self-consistent tracking and from the simulation using the frozen space-charge model after initial 200 turns with 0.05 threshold filtering, 128×128 grid cells, and 25,000 macroparticles. It is seen that emittance growth evolution from the frozen space-charge simulation agrees with that from the self-consistent simulation quite well. The computational speed of the frozen space-charge simulation is about a factor of six faster than the self-consistent simulation in this case.

We also ran the 30 A proton beam through the FODO and sextupole lattice using the frozen simulation and the self-consistent simulation. Fig. 19 shows the 4D emittance growth evolution from the frozen space-charge simulation together with the emittance growth from the self-consistent space-charge simulation with 1.6 million macroparticles and 0.1 threshold filtering. The emittance growth from the self-consistent simulation has converged with respect to the number of macroparticles. In this example, both the frozen space-charge simulation and the self-consistent simulation show emittance growth driven by the third order resonance, while the frozen simulation shows significantly less emittance growth.

Fig. 20 shows the 4D emittance growth evolution of the 1 GeV proton beam through the above FODO and sextupole lattice with 10 A, 20 A, and 30 A beam current from the frozen space-charge simulation. It is seen that with small current, there is little emittance growth caused by the third-order resonance. This is due to the fact that the lattice tune working point is 2.417, and the linear space-charge tune shift 0.038 with 10 A, 0.075 with 20 A, and 0.113 with 30 A current. With the increase of the current from 10 A to 30 A, more and more particles move into the 3rd order (2.333) resonance and results in larger emittance growth as observed in the simulation. The frozen space-charge simulation qualitatively reproduce the physical results of resonance driven emittance growth, which was also observed in the self-consistent space-charge simulation [18].

5. Conclusion

The long-term macroparticle tracking simulation is computationally challenging but needed for the study of space-charge effects in high intensity circular accelerators such as a synchrotron. In this study, we propose using symplectic PIC model with the threshold filtering in frequency domain and frozen space-charge model to address those challenges.

There exists slow numerical emittance growth in the long-term simulation even with the use of symplectic space-charge model. This numerical emittance could be caused by the high frequency density fluctuation or unphysical low frequency density modes associated with the use of small number of macroparticles. In a linear lattice without nonlinear resonance, the artificial emittance growth rate scales inversely as the number of macroparticles when the random sampling error is dominant. In a nonlinear lattice, the artificial emittance growth rate scaling becomes more complicated due to the interaction between the low frequency error and the nonlinear resonance.

The numerical artifacts from macroparticle sampling can be mitigated by the use of threshold filtering in frequency domain. By appropriately choosing threshold value, the numerical emittance growth can be significantly reduced in the long-term simulation. Here, we proposed two types of threshold values. One type of threshold value is a predefined fraction of the maximum amplitude of the charge density spectral distribution. The other type of threshold value is based on the standard deviation of mode amplitude and can be dynamically calculated from the particle distribution in the simulation (this can be computationally expensive). Both types of threshold values yield similar simulation results with appropriate choice of threshold values. The use of numerical filtering is under the situation where significant numerical emittance growth observed in the simulation.

In order to improve the computing speed, we also explored a frozen space-charge model that stores the space-charge potential solutions after some initial time steps and reuse those space-charge potentials in the following long-term simulation. This method significantly reduces the computing time and yields qualitatively reasonable simulation results in comparison to the self-consistent space-charge simulation in the examples used in this study. The frozen space-charge model can be used when the beam charge density does not vary significantly from turn to turn. This corresponds to the situation that the particle beam is not subject to any coherent instability or strong resonance.

Acknowledgments

We would like to thank discussion with Dr. C. Mitchell. This work was supported by the U.S. Department of Energy under Contract No. DE-AC02-05CH11231 and used computer resources at the National Energy Research Scientific Computing Center.

References

[1] A. Friedman, D.P. Grote, I. Haber, Phys. Fluids B 4 (1992) 2203.
[2] H. Takeda, J.H. Billen, Recent developments of the accelerator design code PARMILA, in: Proc. XIX International Linac Conference, Chicago, 1998, p. 156.
[3] S. Machida, M. Ikegami, AIP Conf. Proc, Vol. 448, 1998, p. 73.
[4] F.W. Jones, H.O. Schoenauer, Proc of PAC1999, 1999, p. 2933.
[5] P.N. Ostroumov, K.W. Shepard, Phys. Rev. ST. Accel. Beams 11 (2001) 030101.
[6] J. Qiang, R.D. Ryne, S. Habib, V. Decyk, J. Comput. Phys. 163 (2000) 434.
[7] R. Duperrier, Phys. Rev. ST Accel. Beams 3 (2000) 124201.
[8] J.D. Galambos, S. Danilov, D. Jeon, J.A. Holmes, D.K. Olsen, F. Neri, M. Plum, Phys. Rev. ST Accel. Beams 3 (2000) 034201.
[9] H. Qin, R.C. Davidson, W.W. Lee, R. Kolesnikov, Nucl. Instrum. Methods Phys. Res. A 464 (2001) 477.
[10] G. Franchetti, I. Hofmann, M. Giovannozzi, M. Martini, E. Metral, Phys. Rev. ST Accel. Beams 6 (2003) 124201.
[11] J. Qiang, S. Lidia, R.D. Ryne, C. Limborg-Deprey, Phys. Rev. ST Accel. Beams 9 (2006) 044204.
[12] J. Amundson, P. Spentzouris, J. Qiang, R. Ryne, J. Comput. Phys. 211 (2006) 229.
[13] J. Qiang, R.D. Ryne, M. Venturini, A.A. Zholents, I.V. Pogorelov, Phys. Rev. ST Accel. Beams 12 (2009) 100702.
[14] http://amas.web.psi.ch/docs/opal/opal_user_guide.pdf.
[15] P.J. Channell, C. Scovel, Nonlinearity 3 (1990) 231.
[16] T.J. Stuchi, Braz. J. Phys. 32 (2002) 958.
[17] J. Qiang, Phys. Rev. Accel. Beams 20 (2017) 014203.
[18] J. Qiang, Phys. Rev. Accel. Beams 21 (2018) 054201.
[19] H. Okuda, C.K. Birdsall, Phys. Fluids 13 (1970) 2123.
[20] J. Struckmeier, Phys. Rev. ST Accel. Beams 3 (2000) 034202.
[21] I. Hofmann, O. Boine-Frankenheim, Phys. Rev. ST Accel. Beams 17 (2014) 124201.
[22] O. Boine-Frankenheim, I. Hofmann, J. Struckmeier, S. Appel, Nucl. Instrum. Methods Phys. Res. Sect. A 770 (2015) 164.
[23] F. Kesting, G. Franchetti, Phys. Rev. ST Accel. Beams 18 (2015) 114201.
[24] R.W. Hockney, J.W. Eastwood, Computer Simulation Using Particles, Adam Hilger, New York, 1988.
[25] C.K. Birdsall, A.B. Langdon, Plasma Physics Via Computer Simulation, Taylor and Francis, New York, 2005.
[26] http://mad.web.cern.ch/mad/.
[27] R.D. Ryne, Computational Methods in Accelerator Physics, US Particle Accelerator class note, 2012.
[28] A.J. Dragt, Lie Methods for Nonlinear Dynamics with Applications to Accelerator Physics, 2016.
[29] A.B. Langdon, J. Comput. Phys. 12 (1973) 247.
[30] S. Machida, Proc. of IPAC2015, Richmond, VA, USA, 2015, p. 2402.
[31] H. Bartosik, et al., Proc. of HB2014, East-Lansing, MI, USA, 2014, p. 249.
[32] G. Franchetti, S. Gilardoni, A. Huschauer, F. Schmidt, R. Wasef, Phys. Rev. Accel. Beams 20 (2017) 081006.